(Article begins on next page)

Redox Centers Evolution in Phospho-Olivine Type (LiFe$_{0.5}$Mn$_{0.5}$PO$_4$) Nanoplatelets with Uniform Cation Distribution

Andrea Paolella,[†,‖] Giovanni Bertoni,[†,‡,‖] Enrico Dilena,[†] Sergio Marras,[†] Alberto Ansaldo,[§]

Liberato Manna,[†] and Chandramohan George*,[†]

† Nanochemistry Department, Istituto Italiano di Tecnologia, Via Morego 30, IT-16163 Genova, Italy
‡ IMEM-CNR, Parco Area delle Scienze 37/A, IT-43124 Parma, Italy
§ RBCS Department, Istituto Italiano di Tecnologia, Via Morego 30, IT-16163 Genova, Italy

ABSTRACT

In phospho-olivine type structures with mixed cations (LiM1M2PO4), the octahedral M1 and M2 sites that dictate the degree of intersites order/disorder play a key role in determining their electrochemical redox potentials. In the case of LiFexMn1−xPO4, for example, in micrometer-sized particles synthesized via hydrothermal route, two separate redox centers corresponding to Fe2+/Fe3+ (3.5 V vs Li/Li+) and Mn2+/Mn3+ (4.1 V vs Li/Li+), due to the collective Mn−O−Fe interactions in the olivine lattice, are commonly observed in the electrochemical measurements. These two redox processes are directly reflected as two distinct peak potentials in cyclic voltammetry (CV) and equivalently as two voltage plateaus in their standard charge/discharge characteristics (in Li ion batteries). On the contrary, we observed a single broad peak in CV from LiFe0.5Mn0.5PO4 platelet-shaped (∼10 nm thick) nanocrystals that we are reporting in this work. Structural and compositional analysis showed that in these nanoplatelets the cations (Fe, Mn) are rather homogeneously distributed in the lattice, which is apparently the reason for a synergetic effect on the redox potentials, in contrast to LiFe0.5Mn0.5PO4 samples obtained via hydrothermal routes. After a typical carbon-coating process in a reducing atmosphere (Ar/H2), these LiFe0.5Mn0.5PO4 nanoplatelets undergo a rearrangement of their cations into Mn-rich and Fe-rich domains. Only after such cation rearrangement (via segregation) in the nanocrystals, the redox processes evolved at two distinct potentials, corresponding to the standard Fe2+/Fe3+ and Mn2+/Mn3+ redox centers. Our experimental findings provide new insight into mixed-cation olivine structures in which the degree of cations mixing in the olivine lattice directly influences the redox potentials, which in turn determine their charge/discharge characteristics.

KEYWORDS: Olivine structures, redox energy, platelet shape, nanocrystals, Li ion batteries

Growing energy demand has intensified the efforts to develop strategies for energy storage, and Li ion batteries (LIB) represent one of the most important technologies. Over the last decades of intensive research, phospho-olivine type (LiMPO$_4$) electrode materials, pioneered by Padhi and Goodenough,[1,2] have been identified as serious contenders for high power electrode series. Apart from LiMPO$_4$, other most notable electrode materials are layered LiMnO$_2$ by Bruce and co-workers,[3,4] and LiMSO$_4$OH by Tarascon and coworkers,[5] to name a few. Among the phospho-olivines, LiFePO$_4$ (triphylite) and LiMnPO$_4$ (lithiophilite) are wellknown to form a series of solid-solutions, adopting an orthorhombic crystal structure with Pbnm(62) space group symmetry. Most distinctively, LiFePO$_4$ with a redox potential of 3.4 V versus Li/Li$^+$ is extremely interesting due to its reversible topotactic Li-ion extraction, cyclability, exceptional stability, and flat-voltage characteristics.[6−11] The main reason for such stability stems from the structural features of LiFePO$_4$, being built by stitching of sheets of

FeO$_6$ octahedra and PO$_4$ tetrahedra. In such a structure, the strong covalency of the P$_{tet}$− O bonds in the (PO$_4$)$^{3−}$ tetrahedral polyanion uniquely stabilizes the Fe(3d)−O(2p) antibonds (via an inductive effect), which allows tuning of the M^{2+}/M^{3+} redox energy levels to high voltages, that is, above ∼3.4 V versus Li/Li$^+$ (see Figure 1a,b). This also stabilizes the oxygen atoms in their lattices even in the fully charged state (3.8 V), which makes these Li ion batteries relatively safe. As a result, the structural distortion that can occur during Li ions extraction/insertion (during charge/discharge) is minimal (less than ∼7%) in LiFePO$_4$. LiMnPO$_4$[12] is isostructrual with triphylite and exhibits a redox potential of 4.1 V versus Li/Li$^+$ but is often reported to suffer from poor kinetics upon charge/discharge cycling due to Jahn−Teller active Mn^{3+} ions.[13] When both cations are present, as in LiFe$_{0.5}$Mn$_{0.5}$PO$_4$, the collective Mn− O−Fe interactions[1] (via P$_{tet}$−O−M$_{oct}$) generated in olivine lattices set the redox energy of Mn^{2+}/Mn^{3+} higher than that of Fe^{2+}/Fe^{3+}, because in such lattices the divalent cations (Fe^{2+},

Mn^{2+}) tend to occupy 4c sites, making zigzag chains of corner sharing octahedra (MO$_6$), while Li ions occupy 4a sites (i.e., on edge-sharing octahedral positions).
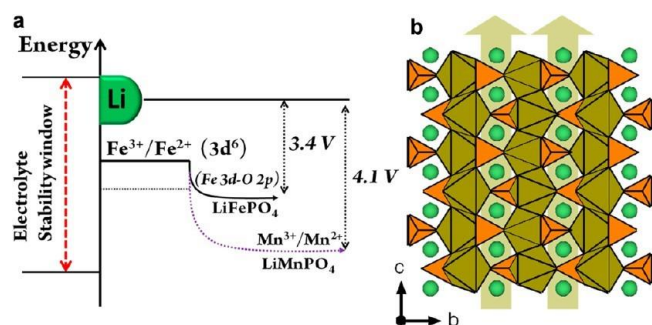

Figure 1. (a) The energy level diagrams, depicting the redox energy of (M$^{2+/3+}$) positions with respect to Li; (b) sketch depicting a [100] view of the olivine type structure for LiFePO$_4$ (triphylite), in which the combination of FeO$_6$ octahedra (brown) and PO$_4$ tetrahedra (orange) results in one-dimensional Li ion (green spheres) channels.

The influence of Mn on the reversible Li ion extraction process in LiFe$_{0.4}$Mn$_{0.6}$PO$_4$ was further detailed by Yamada and co-workers[14,15] by analyzing its phase diagram. During a charge process that removes Li ions, first the Fe^{2+} ions oxidize to Fe^{3+} at ~3.5 V and then at ~4.0 V Mn^{2+} ions oxidize to Mn^{3+}. The sequence is reverted during discharge, that is, during the insertion of Li$^+$ ions, demonstrating two active redox centers in LiFe$_x$Mn$_{(1-x)}$PO$_4$

at 3.4 V: $2LiFe^{+2}_{0.5}Mn^{+2}_{0.5}PO_4 - -Li+ e- \rightarrow 2Li_{0.5}Fe^{+3}_{0.5}Mn^{+2}_{0.5}PO_4$ (1)

at 4.1 V: $2Li_{0.5}Fe^{+3}_{0.5}Mn^{+2}_{0.5}PO_4 - -Li+ e- \rightarrow 2Fe^{+3}_{0.5}Mn^{+3}_{0.5}PO_4$ (2)

Since then, the incorporation of Mn^{2+} into the LiFePO$_4$ lattice within a whole range of LiFe$_x$Mn$_{1-x}$PO$_4$ ($0 \leq x \leq 1$) compositions has been tested by many groups[16–23] and in all cases two different voltage plateaus (~3.5 and ~4.1 V) via two different redox centers were invariably found. The presence of Mn^{2+} in such cases increased both the energy density (by about ~20%) and the capacity with respect to pure LiFePO$_4$, and for this reason the LiFe$_x$Mn$_{(1-x)}$PO$_4$ series of materials has attracted much interest. Obviously, a deeper understanding of these materials in terms of their structural characteristics, such as the nature of cation (Fe, Mn) 4c occupancy sites, Li ion vacancy concentration, intersite order/disorder of 4c sites and phase-segregation in olivine lattices, and the accessibility of any solid-solution regions, is crucial for the optimization of their electrochemical properties. In particular, olivine-type active particles smaller than ~40 nm are known to translate their characteristic two-phase Li insertion/removal processes (flat voltage plateaus) into a single phase reaction (sloping voltage plateau) by minimizing the miscibility gap.[7,24,25] Such roomtemperature single phase reaction is believed to be advantageous over the two phase reaction in reducing the buildup of elastic strain due to the lattice mismatch between LiFePO$_4$ and FePO$_4$ (i.e., between the lithiated and delithiated phases), which might help fast charge/discharge processes.

Here, we report the colloidal synthesis of LiFe$_{0.5}$Mn$_{0.5}$PO$_4$ platelet-shaped nanocrystals (NCs) exhibiting a unique redox behavior with respect to submicrometer crystals of the same material prepared via a standard hydrothermal synthesis: in the nanoplatelets, a single broad peak in cyclic voltammetry (CV) was observed,
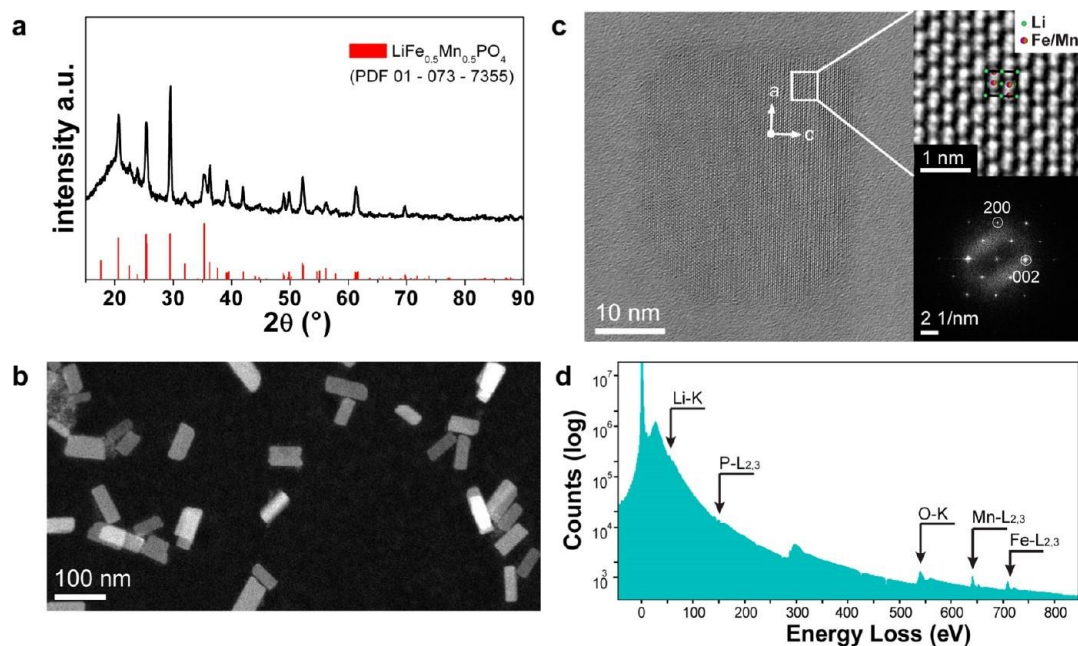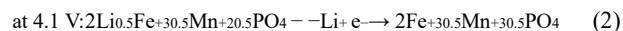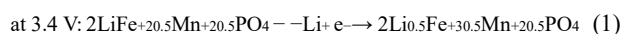

Figure 2. Characterization of the colloidal LiFe$_{0.5}$Mn$_{0.5}$PO$_4$ nanoplatelets. (a) XRD pattern; (b) low-magnification HAADF-STEM image, in which several LiFe$_{0.5}$Mn$_{0.5}$PO$_4$ nanoplates can be seen; (c) HRTEM image of a single nanoplatelet in [010] orientation with a zooming showing the structure with the transition metal atoms dominating the contrast, and the corresponding FFT with the reflections at Bragg conditions; (d) EELS wide spectrum (log-scale) evidencing all the inelastic ionization edges from Li-K, P-L2,3, O-K, Mn-L2,3, and Fe-L2,3. The peak around 285 eV is the CK edge from the carbon thin support film.
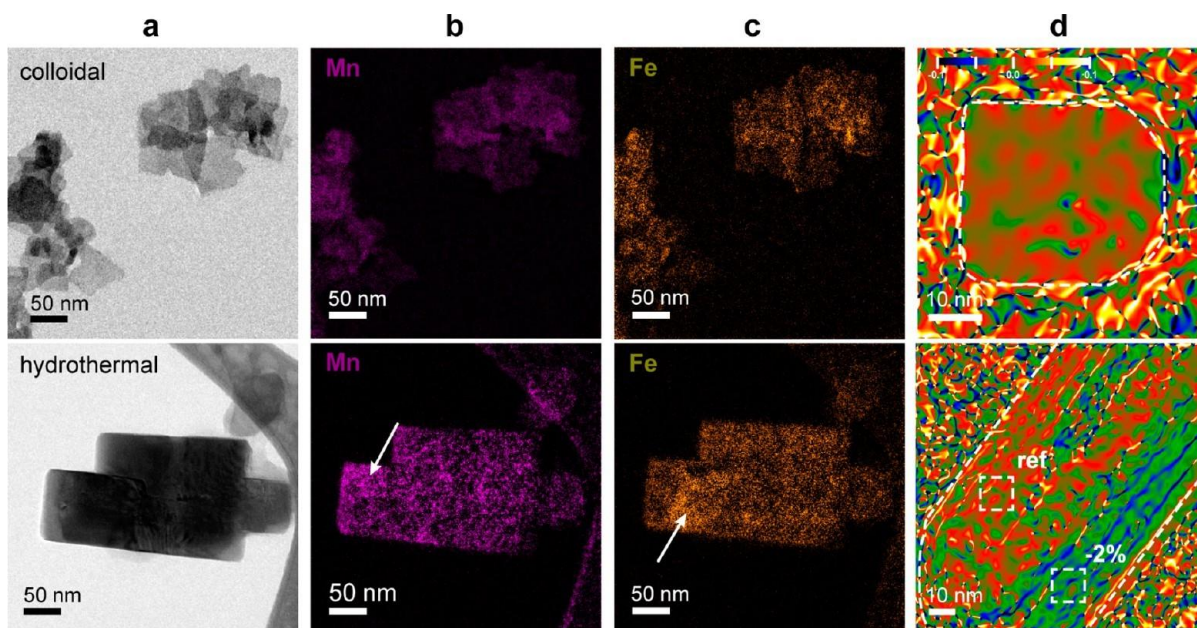
Figure 3. Comparison of the colloidal (top) $LiFe_{0.5}Mn_{0.5}PO_4$ and hydrothermal (bottom) samples. (a) Zero-loss filtered images; (b) Mn maps from the Mn-$L_{2,3}$ ionization edge; (c) Fe maps from Fe-$L_{2,3}$ ionization edge. In the hydrothermal sample, there are regions clearly rich either in Fe or in Mn. On the contrary, there is much better overlap of Fe and Mn maps in the colloidal sample; (d) dilation maps from HRTEM images. The nanoplatelets from colloidal synthesis exhibit uniform dilatation maps (top panel), confirming a good mixing of Fe and Mn atoms also microscopically. On the contrary, in the hydrothermal samples (bottom panel) there are extended regions with approximately 1−2% lattice differences, as expected from $LiFePO_4$ and $LiMnFePO_4$ structural parameters, confirming the partial separation of the two phases.

instead of the two peaks in the hydrothermally prepared sample that are ascribable to the Mn^{2+}/Mn^{3+} and Fe^{2+}/Fe^{3+} redox couples. We demonstrate that this difference is correlated to the difference in the distribution of Fe^{2+} and Mn^{2+} ions in the crystals synthesized with the two methods.

In a typical synthesis of $LiFe_{0.5}Mn_{0.5}PO_4$ nanoplatelets, 0.90 g of lithium iodide, 0.32 g of iron(II) chloride (anhydrous), 0.32 g of manganese(II) chloride (anhydrous), 0.60 g of ammonium phosphate dibasic, 50 mL of oleylamine and 50 mL of 1octadecene were mixed in a 500 mL three-neck flask. The solution was kept under vacuum at 120 °C for 1 h using a standard Schlenk line. It was then heated at 250 °C under N_2 for 3 h. The mixture was transferred to a glovebox and 100 mL of chloroform and 200 mL of ethanol were added. The solution was then centrifuged at 4000 rpm for 20 min. Platelet NCs of either $LiFePO_4$ or $LiMnPO_4$ were prepared in the same way by using the respective precursors for iron or manganese only. The synthetic procedure details are reported in the Supporting Information. The synthesis of submicrometer crystals of $LiFe_{0.5}Mn_{0.5}PO_4$ (with elongated shape, ∼200 nm long and ∼70 nm wide on average) was carried out following a standard hydrothermal synthetic route taken from the literature,[26,27] as described in the Supporting Information.

Structural, morphological, and chemical analyses of the $LiFe_{0.5}Mn_{0.5}PO_4$ platelet NCs prepared via the colloidal synthesis are reported in Figure 2. The NCs were ∼10 nm

thick and ∼70 nm wide. From the XRD pattern (Figure 2a), the structure matches well with lithiophilite, as expected from a mixture of Fe and Mn cations. The broad envelope (around $2\theta = 20°$) in the XRD pattern is typical for this type of NCs (see also Figure S3 and Figure S4 for $LiFePO_4$ and $LiMnPO_4$ colloidal NCs in the Supporting Information), and it is mainly due to the presence of organic residues because the NCs were synthesized using oleylamine as the surfactant, which then coats their surface (as capping layer for the NCs).[28] No other impurity phases were detected in the samples. The lattice constants, as calculated from the XRD spectrum, are a = 4.72 Å, b = 10.50 Å, c = 6.05 Å, very close to the reference structure for lithiophilite (PDF card number 01-073-7355) with Pbnm(62) space group. The low intensity of the (020) reflection with respect to the reference bulk spectrum (Figure 2a) is due to the small thickness of the NCs along the b direction.

Figure 2b is a representative high angle annular dark fieldscanning transmission electron microscopy (HAADF-STEM) image showing a nearly uniform size distribution of the platelet NCs. Figure 2c is a HRTEM image of a single platelet in the [010] zone axis, along with a zoom of the NC, highlighting dominant bright contrast from Mn/Fe cation columns at 4c sites (see the inset), as expected from the phase contrast imaging conditions. The fast Fourier transform (FFT) of the HRTEM image did not show any reflections arising from a superstructural ordering of the transition metal
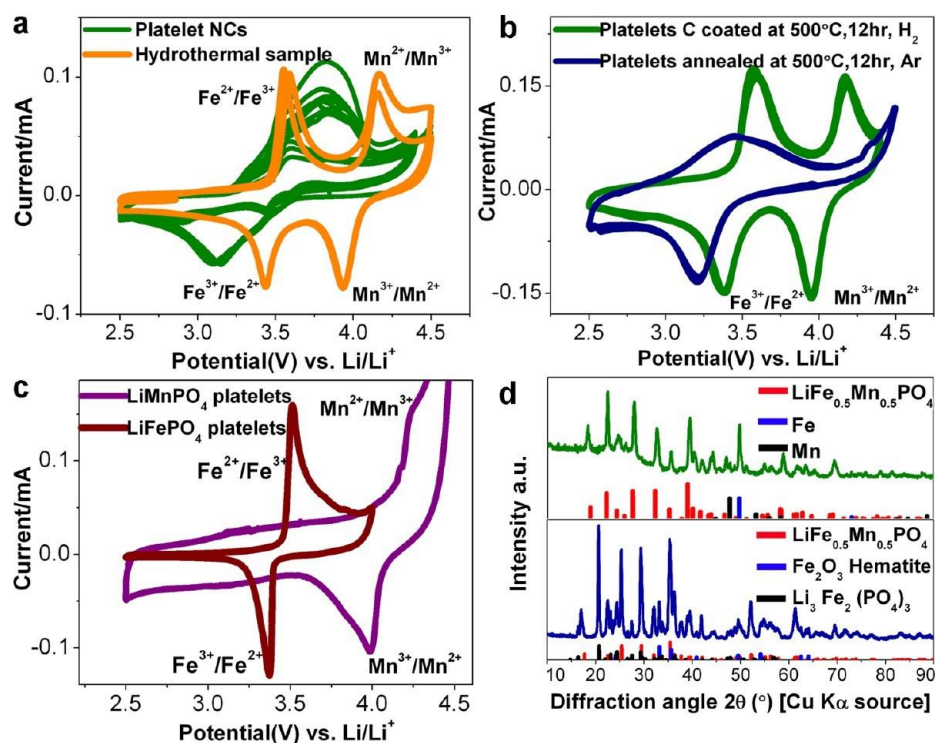
Figure 4. (a) CV response at 0.5 mV/s from colloidal platelet NCs and from hydrothermal NCs under identical conditions; (b) platelet NCs carbon coated at 500 °C for 12 h under Ar/H₂ and platelet NCs annealed at 500 °C for 12 h without H₂; (c) CV response of LiFePO₄ and LiMnPO₄ platelet NCs showing their typical redox at Fe^{2+}/Fe^{3+} at ~3.4 V and Mn^{2+}/Mn^{3+} at ~4.1 V; (d) XRD patterns of the colloidal platelets after carbon coating at 500 °C for 12 h under Ar/H₂ (top) and after annealing at 500 °C for 12 h without H₂ (bottom).

ions. Electron energy loss spectroscopy (EELS) analysis, reported in Figure 2d and obtained by quantifying the intensity of the Mn-$L_{2/3}$ and Fe-$L_{2/3}$ edges averaging many NCs, confirms that the stoichiometry of the NCs sample with respect to Fe and Mn is close to Fe = 0.5 and Mn = 0.5. Energy-dispersive X-ray spectroscopy (EDS) analysis indicates instead a stoichiometry of Mn = 0.45 and Fe = 0.55. The slight difference in composition inferred from the two techniques can be ascribed to the overlap of the Mn-Lβ line with the Fe-Lα line due to the energy resolution (about 140 eV), which can give a systematic overestimation of the Fe signal in EDS. We have also carried out elemental analysis via inductively coupled plasma atomic emission spectroscopy (ICP−AES), which indicated that the ratio Fe/Mn in our samples was close to 1:1 (see Supporting Information). In summary, the synthesized material corresponds to a pure-phase LiFe₀.₅Mn₀.₅PO₄ olivine-type (lithiophilite) crystalline compound. Similar average results (obtained by integrating several tens of crystals) were found on the hydrothermal LiFe₀.₅Mn₀.₅PO₄ samples (see Figure S5 of Supporting Information).

Compositional mapping via energy-filtered TEM (EFTEM) from the colloidal NCs (Figure 3a−c, top panels) indicated that Fe and Mn were well mixed in the NCs, while in the hydrothermal sample there were regions presenting excess of either Mn or Fe (Figure 3a−c, bottom panels, see also the

Supporting Information). We also performed geometric phase analysis (GPA) on both samples.[29] With this technique, it is possible to map local variations in lattice parameter within individual crystals, which can reveal differences in composition, presence of strain, etc. Remarkably, GPA on the colloidal NCs indicated substantial homogeneity in lattice parameter (Figure 3d, top panel), whereas in individual particles from the hydrothermal sample the regions that were Mn-rich regions in the EFTEM maps had 1−2% larger lattice parameter than the Fe rich regions (Figure 3d, bottom panel, see also Supporting Information Figure S2). This difference is in good agreement with the lattice expansion expected in lithiophilite (LiMnPO₄) with respect to triphilite (LiFePO₄). As a note, such difference cannot be seen in XRD patterns where mm² areas are basically averaged.

We then carefully performed CV of both samples in Li metal half cells (2032 coin type, see Supporting Information for further details). The whole processing, including sample preparation and purification, electrode preparation, and cell fabrication, was carefully carried out either in vacuum conditions or in an Ar-filled glovebox in order to avoid any possible side oxidative reactions. Because the redox potential of the olivine structure depends largely on the P_{4c}−O−Fe_{4c} bonding nature, the cations (either Mn or Fe) ordering is very critical in determining their corresponding redox energy. In the case of the hydrothermal
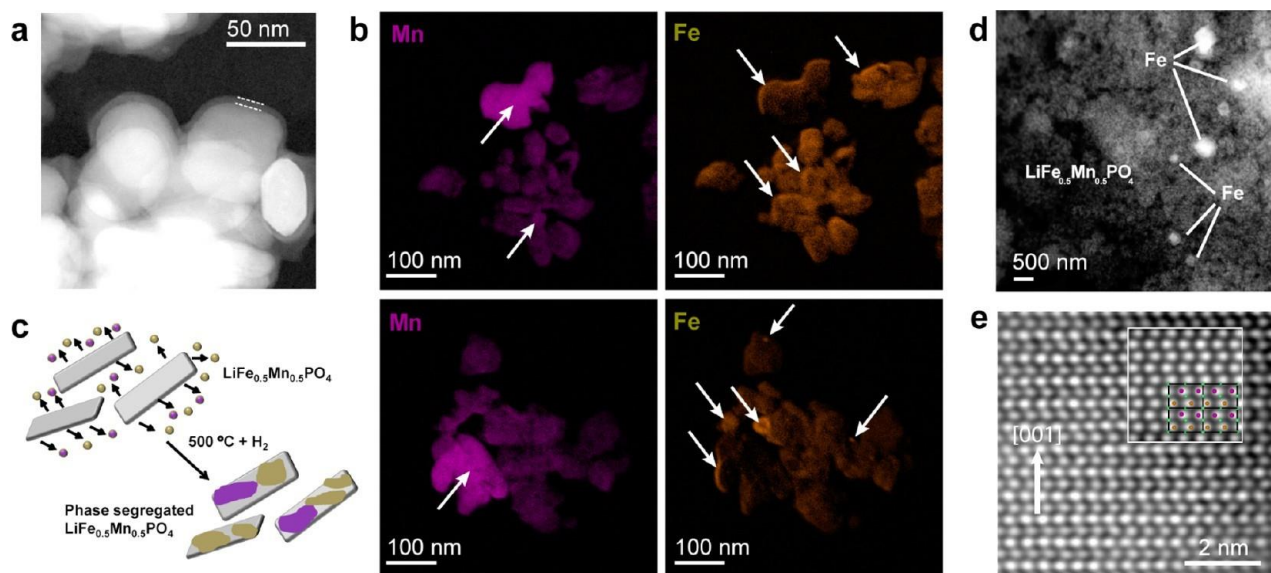
4

Figure 5. (a) HAADF-STEM imaivine structures with mixed cations with other possibt NCs after annealing performed during carbon coating. The NCs are surrounded by a ~4 nm wide carbon shell. (b) EFTEM maps after annealing of the colloidal sample. Both Mn (left) and Fe (right) chemical maps evidence the formation of Mn rich and Fe rich regions in many NCs. Mn rich regions can extend up to entire NCs, while Fe rich parts are often small and close to the edges. (c) Sketch depicting the cations extraction and phase segregation of Fe and Mn in olivine phosphates during a typical carbon coating process. (d) Low-magnification HAADF-STEM image from a dense concentration of colloidal $LiFe_{0.5}Mn_{0.5}PO_4$ after annealing, displaying Fe segregated out of the crystals in the form of metallic Fe clusters. (e) HAADF-STEM at high resolution from a $LiFe_{0.5}Mn_{0.5}PO_4$ NC after annealing. Alternating rows with different contrast are observed. However, a simulation of the image (inset) assuming Mn and Fe ordered rows does not match with the experimental image, pointing to segregation rather than just to alternating cations (see text for details).

$LiFe_{0.5}Mn_{0.5}PO_4$ particles, the CV data (Figure 4a, orange curve) evidenced two distinct redox peaks positioned at 3.5 and 4.1 V, corresponding to Fe^{2+}/Fe^{3+} and Mn^{2+}/Mn^{3+} redox centers. In accordance with the CV data, the corresponding charge/discharge curves, obtained even at 1C rate (~1C = 170 mA/g), are characterized by two plateaus, a first one at about 4.1−3.8 V and a second one at about 3.5 V (see S7 in the Supporting Information), delivering a capacity of ~130 mAh/g with more than ~95% capacity retention. The CV data and charge/discharge curves are therefore in line with the classical redox behavior of olivine type $LiFe_{0.5}Mn_{0.5}PO_4$, where the two different redox centers can be individually accessed. On the other hand, the colloidal NCs differed markedly from the hydrothermal sample both in the CV from which a single broad redox peak could be resolved (Figure 4a, green curve, various cycles are displayed) and in the charge/ discharge curves (see Figure S8 in the Supporting Information). It is worth mentioning here that the CV response and charge/ discharge profiles from electrode materials vs Li/Li^+ are sensitive to the presence of possible impurities, defects, and so forth, because these factors represent different Li^+ ion insertion/removal environments. The CV responses from our NCs were significantly clear in the range from 2.5 to 4.5 V (Figure 4a−c), excluding contributions from impurities. In addition, we did not observe any contribution from organic molecules or from Fe_2O_3. The charge/discharge cycles clearly exhibited only a sloping plateau from 3.9 to 2.5 V (see Figure S8 in the

Supporting Information), instead of the two commonly observed plateaus. This was seen even when working at extremely low scan rates (0.01−0.05C), which in principle should enable to resolve any additional voltage plateau (in contrast to high rates). Moreover, at 0.05C the $LiFe_{0.5}Mn_{0.5}PO_4$ NCs delivered a capacity of ~150 mAh/g with more than ~90% capacity retention. Therefore, the charge/discharge profiles and capacity values indicate that the material is fully crystalline and pure $LiFe_{0.5}Mn_{0.5}PO_4$. The sloping voltage plateau can also indicate the accessibility of the solid-solution regions induced by the size reduction of the active particles (NCs). For example, Nazar and co-workers reported $Na_xFe_{0.5}Mn_{0.5}PO_4$ nanorods with a sloping voltage plateau, which they attributed to the formation of enhanced solid solutions (i.e., a single phase) rather than to kinetic limitations.[30] Furthermore, Persson and co-workers[31] reported that in the case of $LiNi_{0.5}Mn_{1.5}O_4$ (spinel), a single phase reaction of intercalation/deintercalation occurred when various degrees of Ni/Mn cations disorder were introduced in such structure. In order to correlate the observed behavior solely to the possible effect of solid-solutions via a single-phase reaction, we decided to benchmark this behavior with the electrochemical characteristics of the end-members ($LiFePO_4$ and $LiMnPO_4$). We therefore synthesized pure $LiFePO_4$ and pure $LiMnPO_4$ nanoplatelets, following a synthesis procedure similar to that of $LiFe_{0.5}Mn_{0.5}PO_4$. The three samples had comparable dimensions (see Supporting Information for details on

5

synthesis) and were then characterized by CV under identical conditions. Both $LiFePO_4$ and $LiMnPO_4$ platelets exhibited their typical and well-defined redox potential at 3.4 and 4.1 V respectively (Figure 4c), consistent with fully crystalline and pure-phase compounds.[32,33] These well-defined redox peaks are indicative of flat voltage characteristics via two phase reactions (see also Supporting Information). In the light of all these data, the unique behavior of the $LiFe_{0.5}Mn_{0.5}PO_4$ platelets can be explained by considering the rather homogeneous distribution of both cations in the lattices (Figures 3a and 2c). This distribution for a Fe/Mn ratio close to 1:1 is apparently metastable. This could be deduced by observing that under electron beam exposure (even at relatively low doses) we could map clearly the formation of Fe-rich regions in individual nanoplatelets ($LiFePO_4$ and $LiMnPO_4$ are probably more stable than the $LiFe_{0.5}Mn_{0.5}PO_4$ solid solution). Segregation was also observed after thermal annealing of the $LiFe_{0.5}Mn_{0.5}PO_4$ platelet NCs under inert atmosphere (500 °C under Ar for 12 h). XRD patterns of these annealed samples (Figure 4d blue curve) indicated the formation of hematite (Fe_2O_3) domains, similar to what was found upon thermal annealing of $LiFePO_4$ under air.[34] This process should distort heavily the starting nanoplatelets, because besides Fe cations a fraction of oxygen ions must have been extracted (favoring metal oxide formation in the absence of H_2). The CV response from these annealed samples was not in exact match with that of $LiFe_{0.5}Mn_{0.5}PO_4$ as well as with the standard olivine structures with mixed cations with other possible Fe/Mn ratios.[20,22]

On the other hand, we additionally carried out a carbon coating on the starting NCs (which involves a reductive annealing at 500 °C under Ar/H_2 mixture) and monitored the redox peaks positions in CV as a function of annealing time (see Supporting Information Figure S9). After 1 h of carbon coating at 500 °C under Ar/H_2, the samples exhibited a clear peak related mainly to Mn redox centers (Mn^{2+}/Mn^{3+} at 4.1 V) with almost no activity from Fe. This was reflected in the corresponding STEM images, which revealed that mainly Fe cations had diffused out of the NCs, forming Fe metallic grains. The presence of the metallic domains (Fe or Mn) was not observed in the CV measurements, because they are active at potentials well below 2.5 V. After 6 h of annealing, both redox peaks corresponding to Mn^{2+}/Mn^{3+} at 4.1 V and Fe^{2+}/Fe^{3+} at

3.5 V were slightly visible (albeit with a decrease in Mn activity), indicating a continuous cation rearrangement during the carbon coating process.

The two redox peaks (Fe^{2+}/Fe^{3+} at 3.5 V vs Li/Li$^+$) and (Mn^{2+}/Mn^{3+} at 4.1 V vs Li/Li$^+$) were well resolved only after at least 12 h of annealing in carbon coating (Figure 4b, green curve). This time, the response was comparable to that of $Li(Mn_xFe_{1-x})PO_4$/C particles obtained via hydrothermal[35] route at the same Fe/Mn ratio. From the XRD analysis of the 12 h Ar/H_2 annealed sample, reported in Figure 4d (green

curve), we could assess that the sample consisted of a mixture of $LiFe_{0.5}Mn_{0.5}PO_4$ and metallic Fe domains (see also Figure 5d). It is clear that carbon coating under reducing conditions (Ar/H_2 mixture) is necessary in order to enable the cation rearrangement in the nanoplatelets. Indeed, even carbon-coated samples did not give well-defined redox peaks until the cations were sufficiently rearranged upon the removal of excess cations (i.e., those that need to be removed in order to achieve better ordering of the cation columns) as indicated by XRD data (Figure 4d, green curve). Figure 5 reports STEM and EFTEM results from the 12 h Ar/H_2 annealed NCs partly aggregated after the annealing procedure. In particular, a pronounced separation between Mn and Fe rich regions was evident, as shown by the contrast differences in the Mn and Fe maps observed from EFTEM (Figure 5b), similar to what was observed directly in the hydrothermal sample (Figure 3 bottom panels).

This separation between Mn and Fe has to be taken into account when interpreting the CV data. The two peaks in the CV (Figure 4a,b) are related to Fe or Mn preferential channels present in the Fe or Mn rich regions in the samples (see also the sketch of Figure 6). This separation cannot be observed in the original colloidal platelets due to the higher mixing of Mn and Fe atoms in the crystals. Moreover, it is worth noting that in some platelet NCs, after these were annealed for 12 h (under Ar/H_2 during carbon coating), we could observe reflections at g(020)/2 in the HRTEM and HAADF-STEM images (as in Figure 5e). However, the contrast in HAADF images (about 9−10%) was too high to be due to Mn and Fe preferential atomic rows. Simulations (inset of Figure 5e) gave an expected contrast difference of less than 1% that is experimentally undetectable due to the noise in the recorded image. It is likely therefore that the observed contrast originates from ordering of vacancies at the transition metal M2 sites and/or to antisite defects[36,37] (Li atoms occupying Fe/Mn sites and vice versa). Obviously, we cannot rule out completely a contribution to the measured contrast from strain they generate. It is possible that an excess of cations (mainly Fe) from 4c sites had diffused out of the NCs during annealing in H_2, leaving vacancies for Li ions from 4a sites. However, we did not observe any superstructure reflections in XRD data, suggesting that this ordering probably affects only a small region of the crystals. On the other hand, antisite defects may impede the diffusion of Li ions along the 1D channels[38] (also see Figure 1) parallel to the c-axis in olivine. Guo and co-workers[39] were actually able to directly observe Li/Fe antisite defects by using a combination of HAADF-STEM and EELS techniques.

In our case, even if such defects were present in $LiFe_{0.5}Mn_{0.5}PO_4$ they would be possibly eliminated upon cations reordering favored by kinetics at higher temperatures. The removal of antisites defects on $LiFePO_4$ samples has indeed been demonstrated via in situ X-ray diffraction by Jason and co-workers[40] with a post heat treatment at temperatures around ~500 °C. Our NCs
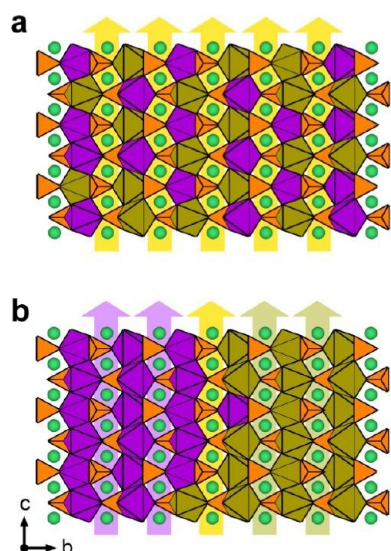
Figure 6. Sketch of the different atomic arrangements around the preferential [001] Li diffusion channels. (a) Colloidal LiFe$_{0.5}$Mn$_{0.5}$PO$_4$ NCs sample before annealing, presenting mixed Mn and Fe atoms surrounding Li channels. Along these channels (yellow arrows) simultaneous redox activities of Mn and Fe atoms are expected. (b) Colloidal LiFe$_{0.5}$Mn$_{0.5}$PO$_4$ NCs after annealing. Li columns are surrounded preferentially by Mn atoms (violet octahedrons) or Fe atoms (brown octahedrons) due to partial phase separation into Mn or Fe rich domains. Along these channels a preferential redox activity of Mn (violet arrows) or Fe (green arrows) is expected.

samples, after an annealing at 500 °C under Ar only, did not give the characteristic two peaks in CV (Figure 4b), meaning that antisites defects cannot be the main factor responsible for the single redox peak. Besides, conventionally, such annealed samples should exhibit a higher degree of crystallinity. Interestingly, the NCs presented the two redox peaks only after carbon coating for 12 h under Ar/H$_2$ (see above). Considering the sequence from the diffusion of transition metals cations (in particular Fe) to their rearrangement and phase-segregation in the NCs during the annealing process involved in the carbon coating, the degree of mixing of the transition metals in the cation columns in LiFe$_{0.5}$Mn$_{0.5}$PO$_4$ platelets NCs is the most likely factor that strongly influences their redox behavior.

In conclusion, we have reported colloidal LiFe$_{0.5}$Mn$_{0.5}$PO$_4$ platelet NCs with the Fe and Mn cations well intermixed. The synthesis effectively prevents cations arrangement into atomic columns with full Fe or Mn occupancies or their phase segregation. During the typical carbon-coating process under Ar/H$_2$, the NCs underwent annealing at 500 °C. EFTEM data revealed a rearrangement of the Fe and Mn cations into domains with preferential Fe or Mn occupation at the M2 sites (i.e., closer to either triphylite or lithiophilite, respectively). CV and charge/discharge profiles of the LiFeMnPO$_4$ NCs have been followed as a function of the annealing time (during the carbon coating process) in order

to study the evolution in the electrochemical properties. The electrochemical data, in conjunction with EFTEM/HRTEM analysis, indicate that cation (Fe and Mn) segregation with respect to the Li ion positions in the olivine lattices is most likely responsible for the distinct activity for both (Fe^{2+}/Fe^{3+} at 3.5 V) and (Mn^{2+}/Mn^{3+} at 4.1 V) redox centers in the olivine type LiFe$_{0.5}$Mn$_{0.5}$PO$_4$ structures. Possible future ways of engineering similar structures would be, for example, the fabrication of nanostructures with target cation arrangements in the olivine lattice or nanostructures with complete phase-segregated dumbbells/dimers or core/shells types of NCs, for optimizing their electrochemical properties in order to achieve better performance.

ASSOCIATED CONTENT

* Supporting Information
Control experiments, synthesis of various types of NCs, their characterizations, and additional electrochemical tests are reported. This material is available free of charge via the Internet at http://pubs.acs.org.

AUTHOR INFORMATION

Corresponding Author
*E-mail: chandramohan.george@iit.it.
Author Contributions
‖A.P. and G.B. contributed equally to this work.
Notes
The authors declare no competing financial interest.

ACKNOWLEDGMENTS

REFERENCES

(1) Padhi, A. K.; Nanjundaswamy, K. S.; Goodenough, J. B. J. Electrochem. Soc. 1997, 144, 1188−1194.
(2) Padhi, A. K.; Nanjundaswamy, K. S.; Masquelier, C.; Okada, S.; Goodenough, J. B. J. Electrochem. Soc. 1997, 144, 1609−1613.
(3) Bruce, P. G.; Armstrong, A. R.; Gitzendanner, R. L. J. Mater. Chem. 1999, 9, 193−198.

(4) Armstrong, A. R.; Bruce, P. G. Nature 1996, 381, 499−500.

(5) Subban, C. V.; Ati, M.; Rousse, G.; Abakumov, A. M.; Van Tendeloo, G.; Janot, R.; Tarascon, J.-M. J. Am. Chem. Soc. 2013, 135, 3653−3661.

(6) Kang, B.; Ceder, G. Nature 2009, 458, 190−193.

(7) Gibot, P.; Casas-Cabanas, M.; Laffont, L.; Levasseur, S.; Carlach, P.; Hamelet, S.; Tarascon, J.-M.; Masquelier, C. Nat. Mater. 2008, 7, 741−747.

(8) Chung, S. Y.; Bloking, J. T.; Chiang, Y. M. Nat. Mater. 2002, 1, 123−128.

(9) Sun, C.; Rajasekhara, S.; Goodenough, J. B.; Zhou, F. J. Am. Chem. Soc. 2011, 133, 2132−2135.

(10) Rui, X.; Zhao, X.; Lu, Z.; Tan, H.; Sim, D.; Hng, H. H.; Yazami, R.; Lim, T. M.; Yan, Q. ACS Nano 2013, 7, 5637−5646.

(11) Gu, L.; Zhu, C.; Li, H.; Yu, Y.; Li, C.; Tsukimoto, S.; Maier, J.; Ikuhara, Y. J. Am. Chem. Soc. 2011, 133, 4661−4663.

(12) Delacourt, C.; Poizot, P.; Morcrette, M.; Tarascon, J. M.; Masquelier, C. Chem. Mater. 2004, 16, 93−99.

(13) Yonemura, M.; Yamada, A.; Takei, Y.; Sonoyama, N.; Kanno, R. J. Electrochem. Soc. 2004, 151, A1352−A1356.

(14) Yamada, A.; Kudo, Y.; Liu, K. Y. J. Electrochem. Soc. 2001, 148, A747−A754.

(15) Yamada, A.; Chung, S. C. J. Electrochem. Soc. 2001, 148, A960− A967.

(16) Hong, J.; Wang, F.; Wang, X.; Graetz, J. J. Power Sources 2011, 196, 3659−3663.

(17) Shin, Y.-J.; Kim, J.-K.; Cheruvally, G.; Ahn, J.-H.; Kim, K.-W. J. Phys. Chem. Solids 2008, 69, 1253−1256.

(18) Chen, L.; Yuan, Y.-Q.; Feng, X.; Li, M.-W. J. Power Sources 2012, 214, 344−350.

(19) Burba, C. A.; Frech, R. J. Power Sources 2007, 172, 870−876.

(20) Wang, Z.-H.; Yuan, L.-X.; Zhang, W.-X.; Huang, Y.-H. J. Alloys Compd. 2012, 532, 25−30.

(21) Zhong, Y.-J.; Li, J.-T.; Wu, Z.-G.; Guo, X.-D.; Zhong, B.-H.; Sun, S.-G. J. Power Sources 2013, 234, 217−222.

(22) Martha, S. K.; Grinblat, J.; Haik, O.; Zinigrad, E.; Drezen, T.; Miners, J. H.; Exnar, I.; Kay, A.; Markovsky, B.; Aurbach, D. Angew. Chem., Int. Ed. 2009, 48, 8559−8563.

(23) Sun, Y.-K.; Oh, S.-M.; Park, H.-K.; Scrosati, B. Adv. Mater. 2011, 23, 5050−5054.

(24) Kobayashi, G.; Nishimura, S.-i.; Park, M.-S.; Kanno, R.; Yashima, M.; Ida, T.; Yamada, A. Adv. Funct. Mater. 2009, 19, 395−403.

(25) Meethong, N.; Huang, H.-Y. S.; Carter, W. C.; Chiang, Y.-M. Electrochem. Solid- State Lett. 2007, 10, A134−A138.

(26) Yao, J.; Bewlay, S.; Konstantionv, K.; Drozd, V. A.; Liu, R. S.; Wang, X. L.; Liu, H. K.; Wang, G. X. J. Alloys Compd. 2006, 425, 362− 366.

(27) Meligrana, G.; Di Lupo, F.; Ferrari, S.; Destro, M.; Bodoardo, S.; Garino, N.; Gerbaldi, C. Electrochim. Acta 2013, 105, 99−109.

(28) Jiang, J.; Liu, W.; Chen, J.; Hou, Y. ACS Appl. Mater. Interfaces 2012, 4, 3062−3068.

(29) Hytch, M. J.; Snoeck, E.; Kilaas, R. Ultramicroscopy 1998, 74, 131−146.

(30) Lee, K. T.; Ramesh, T. N.; Nan, F.; Botton, G.; Nazar, L. F. Chem. Mater. 2011, 23, 3593−3600.

(31) Lee, E.; Persson, K. A. Chem. Mater. 2013, 25, 2885−2889.

(32) Zhu, C.; Yu, Y.; Gu, L.; Weichert, K.; Maier, J. Angew. Chem., Int. Ed. 2011, 50, 6278−6282.

(33) Yang, S.-L.; Ma, R.-G.; Hu, M.-J.; Xi, L.-J.; Lu, Z.-G.; Chung, C. Y. J. Mater. Chem. 2012, 22, 25402−25408.

(34) Hamelet, S.; Gibot, P.; Casas-Cabanas, M.; Bonnin, D.; Grey, C. P.; Cabana, J.; Leriche, J.-B.; Rodriguez-Carvajal, J.; Courty, M.; Levasseur, S.; Carlach, P.; van Thournout, M.; Tarascon, J.-M.; Masquelier, C. J. Mater. Chem. 2009, 19, 3979−3991.

(35) Saravanan, K.; Ramar, V.; Balaya, P.; Vittal, J. J. J. Mater. Chem. 2011, 21, 14925−14935.

(36) Gardiner, G. R.; Islam, M. S. Chem. Mater. 2010, 22, 1242− 1248.

(37) Fisher, C. A. J.; Prieto, V. M. H.; Islam, M. S. Chem. Mater. 2008, 20, 5907−5915.

(38) Nishimura, S.-i.; Kobayashi, G.; Ohoyama, K.; Kanno, R.; Yashima, M.; Yamada, A. Nat. Mater. 2008, 7, 707−711.

(39) Guo, X.; Wang, M.; Huang, X.; Zhao, P.; Liu, X.; Che, R. J. Mater. Chem. A 2013, 1, 8775−8781.

(40) Chen, J.; Graetz, J. ACS Appl. Mater. Interfaces 2011, 3, 1380− 1384.

Redox Centers Evolution in Phospho-Olivine Type (LiFe$_{0.5}$Mn$_{0.5}$ PO$_4$) Nanoplatelets with Uniform Cation Distribution

Andrea Paolella[1‡], Giovanni Bertoni[1,2‡], Enrico Dilena[1], Sergio Marras[1], Alberto Ansaldo[3], Liberato Manna[1] and Chandramohan George[1]*

[1]Nanochemistry Department, Istituto Italiano di Tecnologia, Via Morego 30, IT-16163 Genova, Italy

[2]IMEM-CNR, Parco Area delle Scienze 37/A, IT-43124 Parma, Italy

[3]RBCS Department, Istituto Italiano di Tecnologia, Via Morego 30, IT-16163 Genova, Italy

‡ These authors contributed equally to this work

*chandramohan.george@iit.it

Supporting Information

1.1 Chemicals

Oleylamine (70% *purum*), octadecylamine (97%), octylamine (99%), 1–octadecene (technical grade, 90%), iron (II) chloride anhydrous (99.99%), iron (II) sulfate heptahydrate (99%), manganese (II) chloride anhydrous (99.99%), manganese (II) sulfate heptahydrate (≥99%), ammonium phosphate dibasic (≥99.99%), lithium iodide (beads, ≥99.99%), lithium chloride (anhydrous, 99%), were purchased from Sigma Aldrich. Chloroform and ethanol (anhydrous, 99%) were purchased from Carlo Erba. Cell components for coin type 2032 were purchased from Hohsen Corporation. Polypropylene micro-porous matrixes were purchased from cellguard. Li metal foils were purchased from Goodfellow. Super-P carbon black was purchased from Alfa Aesar. Ethylene carbonate, diethyl carbonate, N-methyl-2-pyrrolidone, (poly)-vinylidene difluoride and carbon powder were purchased from Aldrich. All the solvents used were thoroughly degassed.

1.2 X-ray diffraction (XRD)

XRD spectra were recorded using a Smartlab 9kW Rigaku diffractometer equipped with a copper rotating anode. The X-ray source was operated at 40kV and 150mA. A Göbel mirror was used to obtain a parallel beam and to suppress Cu Kβ radiation (1.392 Å). The 2 theta/omega scan was performed with two radiations, Cu Kα1 (1.544 Å) and Cu Kα2 (1.541 Å), with a step of 0.05° (2θ) and with a scan speed of 3 deg/min. A flat graphite monochromator was used to remove X-ray fluorescence. Specimens were prepared by drop-casting a solution of NCs onto zero-background silicon wafers. The software PDXL by Rigaku was used for qualitative analysis.

1.3 Electrochemical Measurements

All the electrochemical measurements (EC) were carried out using a PARSTAT 2273 potentiostat/galvanostat and a MPG -2 (bio-logic) multi channel battery testing unit.

1.4 ICP-AES Elemental Analysis

Elemental analysis was carried out *via* inductively coupled plasma atomic emission spectroscopy (ICP-AES), using a Varian Vista AX spectrometer. $LiFe_{0.5}Mn_{0.5}PO_4$ NC samples were digested

in HCl/HNO3 3:1 (v/v). The ICP data, for a typical analysis, yielded 46 ppm of Fe and 45 ppm of Mn, therefore a molar ratio of Fe/Mn close to 1:1.

1.5 Transmission electron microscopy (TEM)

High Resolution (HRTEM) and Energy Filtered (EFTEM) images were acquired on a JEOL JEM-2200FS transmission electron microscope with a field emission gun (FEG) operated at 200kV, and equipped with a CEOS imaging corrector operated at Cs ~ -30μm for optimal imaging at high frequencies in HRTEM,[1] and in column Ω-filter for EFTEM, and an Energy Dispersive X-ray Spectrometer (EDS) with a Si(Li) detector. High Angle Annular Dark Field (HAADF) in Scanning Mode (STEM) and Electron Energy Loss Spectra (EELS) were acquired on a FEI TECNAI-G2 FEG microscope at 200kV, equipped with a Gatan Enfinium SE spectrometer. The Mn and Fe ratios were evaluated by making use of EDS and EELS. The first was used to give an average value from areas containing many nanocrystals (thus averaging between Mn and Fe rich regions). Model-based EELS quantification[2] was used to quantify the Mn and Fe contents in the colloidal sample, and give an indication of the errors made in EDS by the superposition of the Mn-Kβ to the Fe-Kα. EDS seems to give an overestimation of Fe of +5% due to the overlap.

Table 1. *Energy Dispersive Spectroscopy (EDS) estimation of Mn and Fe contents in*
$LiFe_{0.5}Mn_{0.5}PO_4$ samples.

$LiFe_{0.5}Mn_{0.5}PO_4$	Mn-Kα	Fe-Kα	Mn-L$_{2,3}$	Fe-L$_{2,3}$
Hydrothermal	45%	55%	--	
Colloidal	44%	56%	49(1)%	51(1)%
Colloidal annealed (see 1.8)	43%	57%	--	

In 3d transition metals the L$_3$ and L$_2$ intensity depends on the occupancy of the 3d bands, and can be used (with limitations) to derive the oxidation state of the atom.[3] We followed the procedure described in [3] to extract the white-line ratio from the L$_{2,3}$ edge. Briefly, we applied a power-law background subtraction, followed by a deconvolution with a low-loss spectrum, and subtraction of a Hartree-Slater cross-section fitted in the region beyond the white-lines. The

resulting white-lines were integrated in a 7eV energy window. Mn shows indeed a monotonic relation of its oxidation state with the Mn-$L_{2,3}$ white-line ratio. A value close to 3.8 (according to equation 1 in ref. [3]) is a signature of a +2 oxidation state, while a value close to 2.3 is related to a +3 state. Unfortunately the same cannot be applied to Fe, which does not show a monotonic relation.
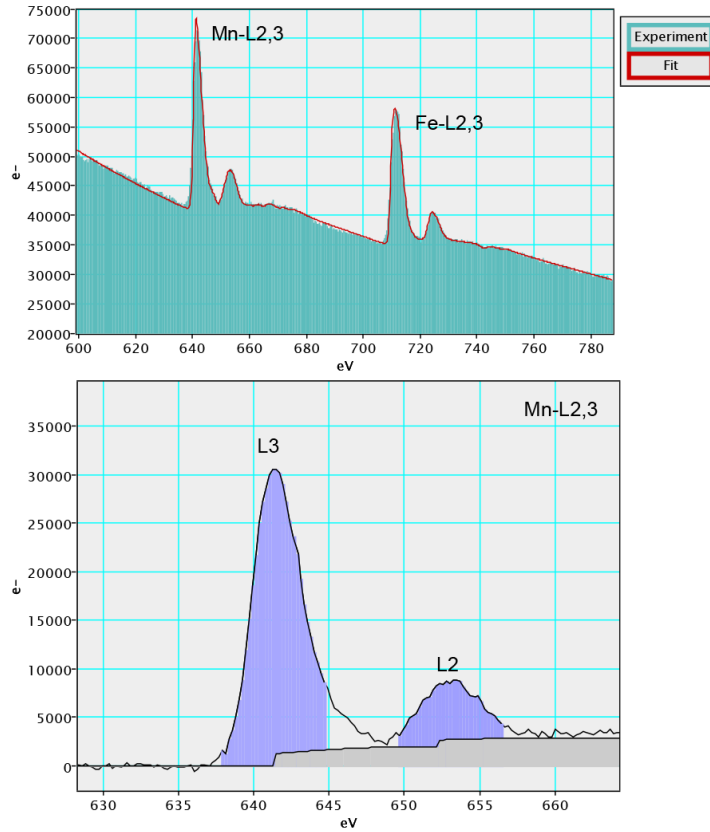

Figure S1. *(Top) Result of model-based fitting of the EELS spectrum for the Mn-$L_{2,3}$ and Fe-$L_{2,3}$ in colloidal LiFe$_{0.5}$Mn$_{0.5}$PO$_4$ platelet NCs. The fitted curve (red) is superimposed to the experimental data. (Bottom) The white-line ratio is determined as the ratio of the two light-blue integrated regions (7 eV wide) after background subtraction and deconvolution of the spectrum. Mn is shown as an example.*

Table 2. *Energy Loss Spectra (EELS) for determining the oxidation state of Mn and Fe in* $LiFe_{0.5}Mn_{0.5}PO_4$ *platelet NCs*

$LiFe_{0.5}Mn_{0.5}PO_4$	$Mn\ L_3/L_2$ (oxidation state)		$Fe\ L_3/L_2$
Hydrothermal	4.04	(+1.91)	4.20
Colloidal	3.97	(+1.94)	4.06
Colloidal annealed (see 1.8)	4.04	(+1.91)	3.74

All the extracted Mn ratios are compatible with a +2 oxidation state. For iron (Fe) we found very similar values (compatible with +2 states). The lower ratio in the annealed sample was probably due to the presence of Fe (0) due to metal (mainly Fe compared to Mn) extraction during the H_2 annealing (see Section 1.8). As a result, in all samples the Mn atoms (and probably Fe atoms) maintain their +2 oxidation state. In order to verify the structural variation corresponding to Fe and Mn phase separation, we compared RFTEM maps with dilatation maps from Geometric Phase Analysis (GPA), using the FRWR tools plugin for DigitalMicograph™ by Prof. C. Koch.[4]
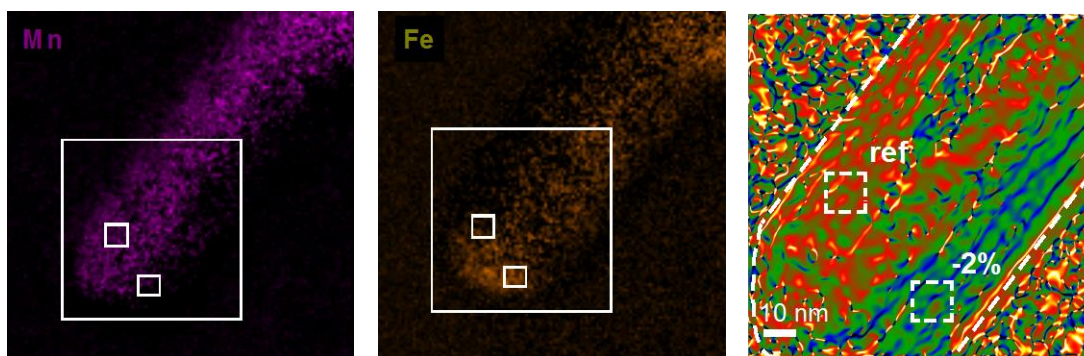

Figure S2. *Mn and Fe chemical maps obtained from EFTEM compared with GPA dilatation map. There is a correspondence between the Mn rich region (higher left portion of the image) and the Fe rich region (lower right portion) and the structural difference expected (larger lattice constant for Mn lithiophilite with respect to Fe triphylite).*

1.6 Colloidal synthesis of LiFePO₄ nanoplatelets

In a typical synthesis of LiFePO$_4$ nanoplatelets 0.90 g of lithium iodide, 0.63 g of iron (II) chloride, 0.60 g of ammonium phosphate dibasic, 50 ml of oleylamine and 50 ml of 1-octadecene were mixed in a 500 ml three neck flask. The solution was kept under vacuum at 120°C for 1 hr using a standard Schlenk line. After that, it was heated at 250˚C under N$_2$ for 3 hours. The mixture was transferred to a Glove Box and 10 ml of chloroform and 20 ml of ethanol were added to it. The solution was then centrifuged at 4000 rpm for 20 minutes.
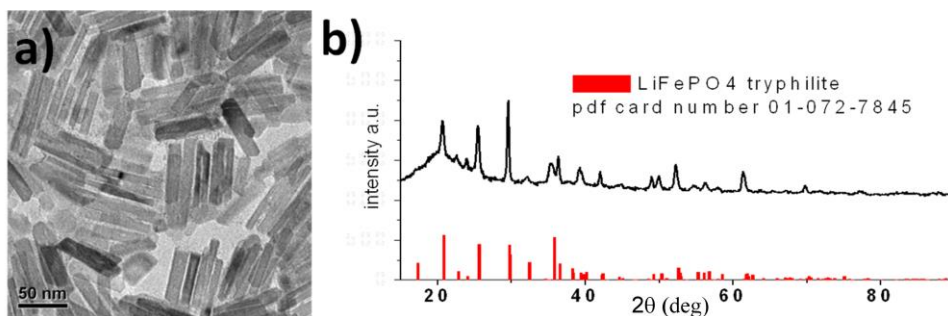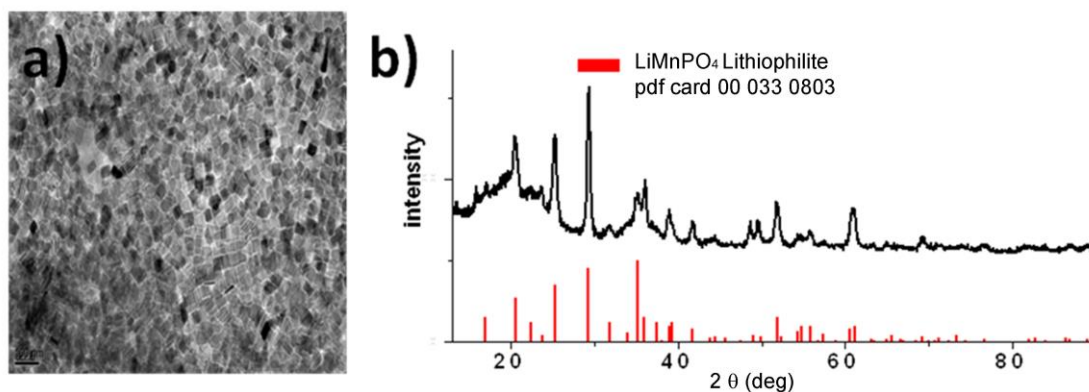

Figure S3. *a) TEM image and b) XRD pattern collected on a sample of LiFePO$_4$ nanoplatelets.*

1.7 Colloidal synthesis of LiMnPO₄ nanoplatelets

In a typical synthesis of LiMnPO$_4$ nanoplatelets 0.90 g of lithium iodide, 0.61 g of manganese (II) chloride, 0.60 g of ammonium phosphate dibasic, 50 ml of oleylamine and 50 ml of 1-octadecene were mixed in a 500 ml three neck flask. The solution was kept under vacuum at 120°C for 1 hr using a standard Schlenk line. After that, it was heated at 250˚C under N$_2$ for 3 hr. The mixture was transferred in Glove Box and 10 ml of chloroform and 20 ml of ethanol were added to it. The solution was then centrifuged at 4000 rpm for 20 minutes.

Figure S4. *a) TEM image and b) XRD pattern collected on a sample of LiMnPO$_4$ nanoplatelets.*

1.8 Hydrothermal synthesis of $LiFe_{0.5}Mn_{0.5}PO_4$ sub-micron crystals

The synthesis of $LiFe_{0.5}Mn_{0.5}PO_4$ elongated submicron particles was performed following a slightly modified version of Yao *et al.*[5] In a typical synthesis, 0.75g of $FeSO_4*7H_2O$, 0.65g of $MnSO_4*H_2O$, 0.3g of L-ascorbic acid, and 0.55g of phosphoric acid (85 wt. %) were dissolved in 50mL of milli-Q water and stirred in a 150 mL beaker for 15 min. About 4 ml of octylamine were added to the mixture in order to keep the size of the crystals in the sub-micron range. In a separate beaker 0.89g of anhydrous LiOH was dissolved in 20 mL milli-Q water. The lithium solution was slowly added to the previous mixture and the resulting solution was then transferred into a quartz glass inside the hydrothermal reactor and mechanically stirred. The reaction temperature was set to 175°C for 18 hr. The particles were separated from the supernatant by centrifugation and were washed several times with distilled water and ethanol.
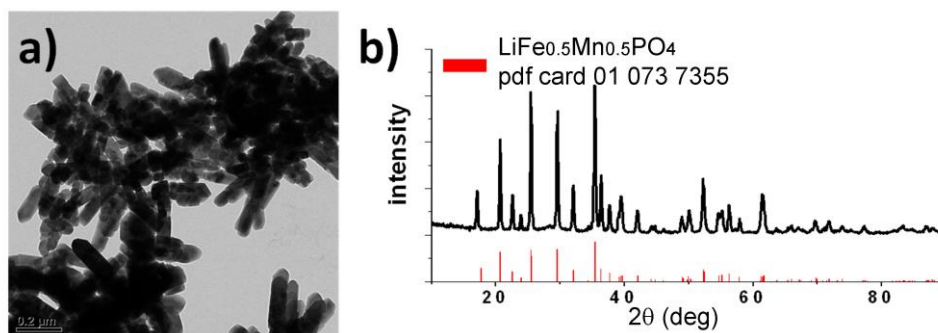

Figure S5. *a) TEM image and b) XRD pattern collected on a sample of hydrothermal $LiFe_{0.5}Mn_{0.5}PO_4$ sub-micron crystals.*

1.9 Annealing experiments of $LiFe_{0.5}Mn_{0.5}PO_4$

Annealing experiments were performed in a quartz tube (120 cm length and 25 mm inner diameter) passing through a three zones split furnace (PSC 12/--/600H, Lenton, UK). Gas flows were controlled upstream by an array of mass flow controllers (1479A, mks, USA) having different ranges and regulated by a multichannel gas flow & pressure controller (type 647C, mks, USA). The gases were first flown to a specific mass flow controller by a valve matrix 5x6 (5 gas inlets, 6 outlets) and then mixed before entering the furnace. Furnace operation and gas mixtures were controlled by a custom LabVIEW (National Instruments, USA) based software.

The carbon coating process of the $LiFe_{0.5}Mn_{0.5}PO_4$ nanoplatelets was performed as follows. A quartz combustion boat containing the NC samples (prepared mixing $LiFe_{0.5}Mn_{0.5}PO_4$

nanoplatelets and 20wt % of glucose) was placed in the middle of the furnace while flowing 50sccm of argon (Ar) gas. The temperature was then slowly (15°C/min) raised up to 450°C and up to 500°C (10°C/min). The slow heating process was chosen to avoid temperature overshoots, and the heating procedure took about 35min. After that, the sample was kept at constant temperature (500°C) in 50 sccm of forming gas (95% Ar, 5% H_2) in order to enhance the iron segregation or under pure Ar (to evaluate the mere thermal effect on iron segregation). After 1, 3, 6 or 12 hrs, depending on the experiment, the furnace was switched off and allowed naturally to cool down while still keeping the samples in a 50sccm flow of Ar. Similarly, the hydrothermal $LiFe_{0.5}Mn_{0.5}PO_4$@C sample was prepared by mixing $LiFe_{0.5}Mn_{0.5}PO_4$ sub-micron crystals with 20% glucose. The final mixture was heated at 500°C for 12 hr under forming gas (95% Ar, 5% H_2).

Figure S6*. A Photo showing our furnace set-up used for the carbon coating and annealing experiments.*

1.10 Battery fabrication and Electrochemical Measurements

All the steps of the battery fabrication were carried out in an Ar filled glove box. First of all, the samples of $LiFe_{0.5}Mn_{0.5}PO_4$, $LiMnPO_4$, and $LiFePO_4$ platelet NCs were repeatedly washed with a 1:1 mixture of ethanol and toluene. The precipitated material was then allowed to dry overnight. $LiFe_{0.5}Mn_{0.5}PO_4$ elongated submicron particles (obtained *via* hydrothermal route) were washed several times with distilled water and ethanol, followed by drying in an oven for 24 hr. The dried powder was then mixed with Super-P carbon black and polyvinylidene difluoride (PVDF) in N-methyl-2-pyrrolidone (degassed), such that the weight fraction of NCs in the resulting mixture was about 75%. The vial containing the mixture was ground well and stirred for about 2 hr in order to obtain a homogeneous slurry. Then the NCs slurry was applied onto the current

collector, dried at 120°C for overnight, and then pressed, which resulted in a uniform and compact coating. Coin type 2032 cells were assembled with the coated current collector serving as one electrode, while a pure Li metal disk served both as reference and counter electrode. A solution of 1M lithium hexafluorophosphate (in 1:1:1v% propylene carbonate, ethylene carbonate and diethyl carbonate) was used as electrolyte and polypropylene layers were employed to separate the electrodes.
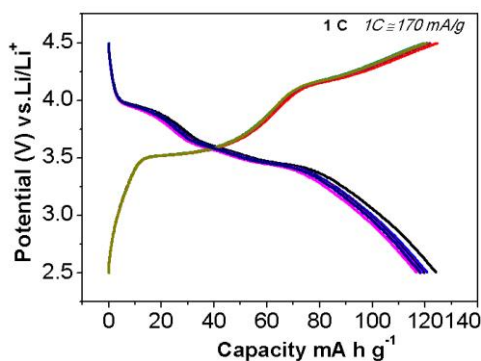

Figure S7. *Charge/discharge profiles from hydrothermal $LiFe_{0.5}Mn_{0.5}PO_4$ samples at 1C rate. Even at such high rate the two voltage plateaus can be observed clearly.*
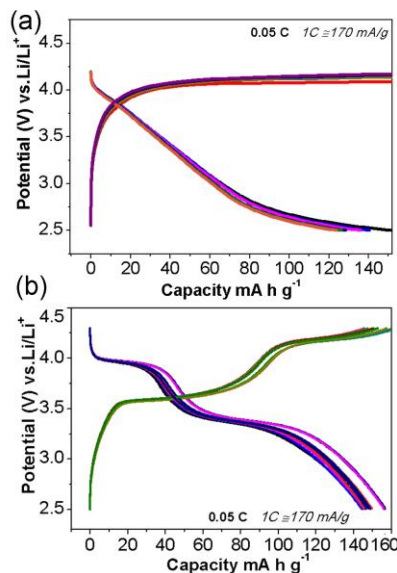

Figure S8. *Charge/discharge profiles acquired carefully at low rate (0.05 C) which enables a clear monitoring of the voltage plateaus upon the Li ions extraction/insertion of: a) colloidal $LiFe_{0.5}Mn_{0.5}PO_4$ nanoplatelets before annealing in the carbon coating process; b) after carbon coating at 500°C for 12 hr under H_2.*
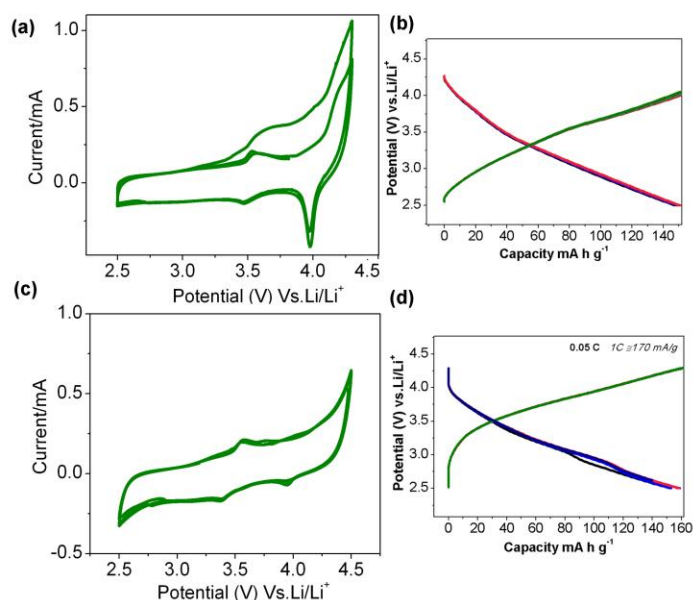
Figure S9. *Cyclic voltammetry (CV) acquired at 0.5 mV/s and charge/ discharge profiles acquired at a 0.05 C rate for annealed LiFe₀.₅Mn₀.₅PO₄ platelet NCs in the carbon coating process at 500°C under Ar/H₂ as a function of time: a-b) after 1 hr, c-d) 6 hr. The changes in the redox peaks in CV and their corresponding voltage plateaus indicate that the cations re-arrangement processes did take place in the NCs during the carbon coating process.*
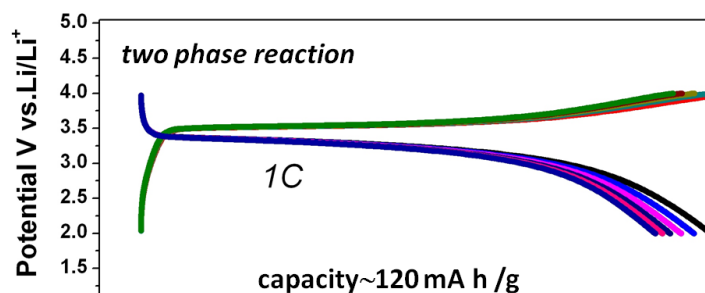

Figure S10. *Charge/ discharge profiles acquired at 1C rate on LiFePO₄ platelet NCs (sizes and shapes were comparable to those of the LiFe₀.₅Mn₀.₅PO₄ platelet NCs), evidencing their characteristic two phase Li ions insertion/removal upon charge/discharge cycles. The NCs had delivered a capacity ~120 mAh/g with ~95% capacity retention.*
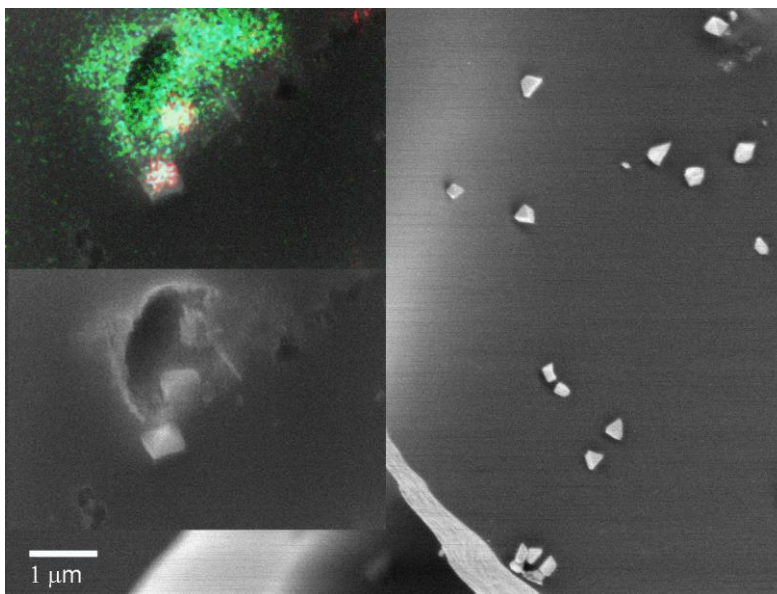
S10

Figure. S11 *SEM image showing the metal particles found in samples annealed at 500 °C, Ar/H$_2$, for 12 hr, with insets of SEM-EDS elemental map (colour coding: red (Fe), turquoise (Mn), green (P), as supported by the XRD data of the manuscript (in Figure. 4d).*

References:

(1). Bertoni, G. ; Grillo,V.; Ke.X.; Bals, S.; Catellani, A. ; Li,H.; Manna, L. *ACS Nano,* **2012**, 6, 6453–6461.

(2). Bertoni, G.; Verbeeck, J. *Ultramicroscopy,* **2008**, 108 ,782–790.

(3). Tan, H.; Verbeeck, J.; Abakumov, A.; Van Tendeloo, G. *Ultramicroscopy*, **2012**, 116, 24–33.

(4). FRWRTools plugin. http://elim.physik.uni-ulm.de

(5). Yao, J.; Bewlay, S.; Konstantionv, K.; Drozd, V. A.; Liu, R. S.; Wang, X. L.; Liu, H. K.; Wang, G. X. *J. Alloys Compd.* **2006**, 425, 362–366.